Nuclear Materials and Energy 25 (2020) 100860

Contents lists available at ScienceDirect

Nuclear Materials and Energy

journal homepage: www.elsevier.com/locate/nme

Modeling of COMPASS tokamak divertor liquid metal experiments

J. Horacek [a,*], R. Dejarnac [a], J. Cecrdle [b], D. Tskhakaya [a], A. Vertkov [h], J. Cavalier [a], P. Vondracek [a], M. Jerab [a], P. Barton [a], G. van Oost [c,f,g], M. Hron [a], V. Weinzettl [a], D. Sestak [a], S. Lukes [b], J. Adamek [a], A. Prishvitsin [c], M. Iafratti [e], Y. Gasparyan [c], Y. Vasina [c], D. Naydenkova [a], J. Seidl [a], E. Gauthier [d], G. Mazzitelli [e], M. Komm [a], J. Gerardin [a], J. Varju [a], M. Tomes [a], S. Entler [a], J. Hromadka [a], R. Panek [a]

[a] Institute of Plasma Physics of the CAS, Prague, Czech Republic
[b] FNSPE, Czech Technical University, Prague, Czech Republic
[c] National Research Nuclear University MEPhI, Moscow, Russia
[d] CEA, IRFM, F-13108 Saint-Paul-lez-Durance, France
[e] ENEA, Fusion Technology Division, Frascati, Italy
[f] Ghent Universit y, Ghent, Belgium
[g] National Research University Moscow Power Engineering Institute, Moscow, Russia
[h] JSC Red Star, Moscow, Russia

ARTICLE INFO

Keywords:
Tokamak
Divertor
Liquid metals
Plasma facing components

ABSTRACT

Two small liquid metal targets based on the capillary porous structure were exposed to the divertor plasma of the tokamak COMPASS. The first target was wetted by pure lithium and the second one by a lithium-tin alloy, both releasing mainly lithium atoms (sputtering and evaporation) when exposed to plasma. Due to poorly conductive target material and steep surface inclination (implying the surface-perpendicular plasma heat flux 12–17 MW/m^2) for 0.1–0.2 s, the LiSn target has reached 900 °C under ELMy H-mode. A model of heat conduction is developed and serves to evaluate the lithium sputtering and evaporation and, thus, the surface cooling by the released lithium and consequent radiative shielding. In these conditions, cooling of the surface by the latent heat of vapor did not exceed 1 MW/m^2. About 10^{19} lithium atoms were evaporated (comparable to the COMPASS 1 m^3 plasma deuterium content), local Li pressure exceeded the deuterium plasma pressure. Since the radiating Li vapor cloud spreads over a sphere much larger than the hot spot, its cooling effect is negligible (0.2 MW/m^2). We also predict zero lithium prompt redeposition, consistent with our observation.

1. Motivation for better power-handling divertor targets

Development of plasma scenarios, which would be compatible with material limits (surface-perpendicular divertor target heat flux $q_{dep} = 15 \pm 2.5$ MW/m^2, see Fig. 18 in [25]) of conventional divertor modules, is a challenging active field of research, especially with respect to conditions expected in ITER and the European DEMO concept [36,37]. For instance, the plasma heat flux in attached L-mode in ITER is expected to be already around $q_{dep} = 10$ MW/m^2 [17]. In attached ELMy H-mode $Q_{fusion} = 10$ ITER, [12] empirically predict $40 < q_{\perp}$[MW/m^2] < 200, whilst sophisticated simulation approach [25] yields (for impurity-seeded detached plasma) marginally acceptable $4 < q_{dep}$[MW/m^2] < 30. For the European DEMO2, even higher $q_{dep} \sim P_{SOL}B_{tor}/R_0$ could be reached due to higher 200 MW $< P_{SOL} = P_{fusion}/5 <$ 650 MW unless extreme levels of power dissipation is achieved. In addition, flash melting of the entire divertor tungsten surface could happen regularly on ITER by Type-I ELMs according to the scaled ELM energy divertor fluence [40][2] because ELMs appear to easily burn through the detached plasma even with impurity-seeding [20] which otherwise detach well the L-mode [19].

A promising alternative to conventional solid metals are liquid metal divertor (LMD) targets. Liquid metals aim to handle especially the transient heat pulses (ELMs, disruptions) and may also be combined with other heat flux dissipation means such as resonant magnetic perturbations or fast strike-point sweeping [15]. Compatibility of liquid metal plasma facing components have been demonstrated on linear

* Corresponding author.
E-mail address: horacek@ipp.cas.cz (J. Horacek).

https://doi.org/10.1016/j.nme.2020.100860
Received 31 July 2020; Received in revised form 25 September 2020; Accepted 23 November 2020
Available online 30 November 2020

plasma devices or limiter tokamaks under both steady-state and in plasma heat pulses (c.f. Table 1 in [16]), but never successfully in the divertor region under ELMy H-mode, which is therefore studied here.

2. High heat flux experimental test on the COMPASS tokamak

By means of a small LMD target (its design described in [16]) with cylindrical surface at steep angle ($q_{dep} < ¾ q_{||}$) to the incident plasma heat flux (see Fig. 1), ITER-relevant surface heat flux density was reached on the COMPASS tokamak. Due to the target cylindrical shape and the insertion z^{LMD}, the plasma incident angles α vary along the toroidal coordinate (see Fig. 2c in [8]) such that the maximum deposited heat flux is expected at the magnetic shadow edge. Note that, in contrast to the cylindrical limiter used in FTU [39], in divertor plasma the heat flux arrives from only one direction (this is why the COMPASS LMD target shape is ¼ of a cylinder) and that $q_{||}$ does not decrease toroidally away from the top along the target (whilst on FTU it does because it forms the scrape-off layer). Since on COMPASS the discharge time is rather short (0.2 s), we used poorly-conductive bulk material of the LiSn target to rapidly raise the surface temperature, getting thus marginally close to the desired lithium-vapor-shielded steady-state similarly to [24]. The target is designed in such a way that the liquid was wetted in a 1 mm-thick mesh knitted from 0.1 mm thin molybdenum wires (see Fig. 1 in [8]) forming a *capillary-porous structure* (CPS) [34]. Evaporated liquid refills from the wet CPS and internal reservoir by the natural capillary forces, strong enough to also hold droplets splashing off the surface. For more insights on the realized experiment, the reader is referred to [8], where the LMD target geometry, the main plasma discharge parameters, the steady divertor heat flux profiles, lithium spectroscopy and thermovision of the target surface are presented. Post-mortem analysis of the deposited lithium across the vessel is presented in [32]. Note that for the first campaign pure lithium was used, while lithium-tin (*LiSn*) alloy was used in the 2nd campaign. The major advantages (which we observed) of using LiSn alloy instead of Li is that LiSn does not oxidize [22] (due to low chemical activity of this alloy to air and water vapor compared to pure Li). LiO is a powder-like solid substance (we observed it) which likely caused the Li target damage by preventing the undersurface liquid Li to wet the surface, described in Section 5.2. In addition, LiSn evaporates only pure Li (which is ~800x weaker radiator [38, page 231] than Sn), it is the same as Li but for temperature higher by + 310 K. Also, Tin easily redeposits since its ion Larmor radius is comparable to the mean free path. Indeed, our SXR signals and tomography reconstruction by AXUV in the core did not observe any heavy (Sn) element while the LiSn target was inserted. Postmortem analysis of steel screws surface revealed lots of Lithium deposits but Tin was not observed (possibly due to interference with Ni, Cr and Fe lines) [32]. Additionally, the SOL profiles measured at midplane were not perturbed when the LiSn target was inserted in L-mode.

Even though the target was observed by the fast infrared camera, the surface emissivity was not known and varying during the first lithium campaign, due to progressive removal of an oxidized layer covering the target. Calibration was possible only for the LiSn campaign by tile-embedded thermocouples.

In this paper, we concentrate on comparing those experimental observations with a simulation of the LMD surface temperature, implying the consequent lithium sputtering, evaporation, radiation in the SOL plasma and of the subsequent cooling of the surface, even during the ELM heat pulses.

3. Heat conduction simulation and lithium vapor shielding

The aim of the simulation described below is to model the target surface temperature $T_{surface}$ and evaporation rate (lithium pressure p_{Li}) using the measured incident local deuterium plasma temperature T_e and density n_e and its material properties. For that, three different mechanisms A B C were accounted for.

A. Heat conduction into the material dominantly determines the LMD temperature. We improved the general model described in [16] of time-evolving 3D heat solid-body conduction: $\frac{\partial T}{\partial t} = -\frac{1}{c_v}\nabla\cdot(\nabla(kT))$ by incorporating the effects described in **B** and **C**.

The greatest uncertainty in the simulation is the poorly known heat conductivity κ and capacity c_v (which are temperature dependent) of the CPS-wetted liquids, see Table 1. We tested their consistency by a long after-shot surface cooling, which is determined mainly by the LMD bulk material properties. We *do not* simulate movement of the liquid (as e.g. in Fig.7 in [41]) and anyway in the LiSn experiments the liquid visibly did not move at all (in contrast to the pure lithium slipping on the oxidized layer as described in [8]).Fig. 3

The model boundary condition is q_{dep} measured by one of these two techniques:

- **divertor probes** [resolution 3 mm, 10^{-6} s] as $q_{dep}^{probes} = \gamma sin(\alpha) j_{sat} T_e$ with $\gamma = 11$ the sheath heat transmission coefficient matching $q_{dep}^{IR} = q_{dep}^{probes}$ in both steady-state phase (Fig.4 in [8]) and even during ELMs (Fig. 2).
- **infrared (IR) camera** [resolution ½ mm, 10^{-4} s] observing the infrared light emitted by the graphite tile (with high and well known emissivity) [35] just 2 cm toroidally in front of the target and with fixed 3° incidence angle (plus 1° ± 0.1° depending on plasma current due to fieldline inclinations), processed by the Theodor code [14] to obtain heat flux q_{dep}^{IR}.

B. Cooling by latent heat of vapor [6]: A *lithium* atom needs $E_{vap} =$

Table 1
Material properties considered in the simulations. Note that the influence of the Molybdenum mesh on the liquid metal heat conductivity was neglected because the mesh wires are knitted parallel to the surface (see Fig. 1 in [8]), allowing negligible conduction through the Molybdenum below the surface. Properties of the mixed materials (BNC and LiSn) are calculated according to the additive rule.

Material properties	lithium	27% Li + 73% Sn alloy	*Molybdenum*	80% **BN** + 20% B_4C ceramic BNC
used for the	wetted 1mm thin *Mo* CPS layer		20 mm thick bulk LMD target	
heat capacity c_v [J/K/cm^3]	2.24 [11]	1.6 for 800 C [28]	2.6 [9]	2.57
heat conductivity κ [W/m/K]	38+T[°C]/35 [28]	27+T[°C]/40 [28]	145-T[°C]/33 [26]	15-17
melting [°C]	180.5	330	2623	-----

(See above-mentioned references for further information.)

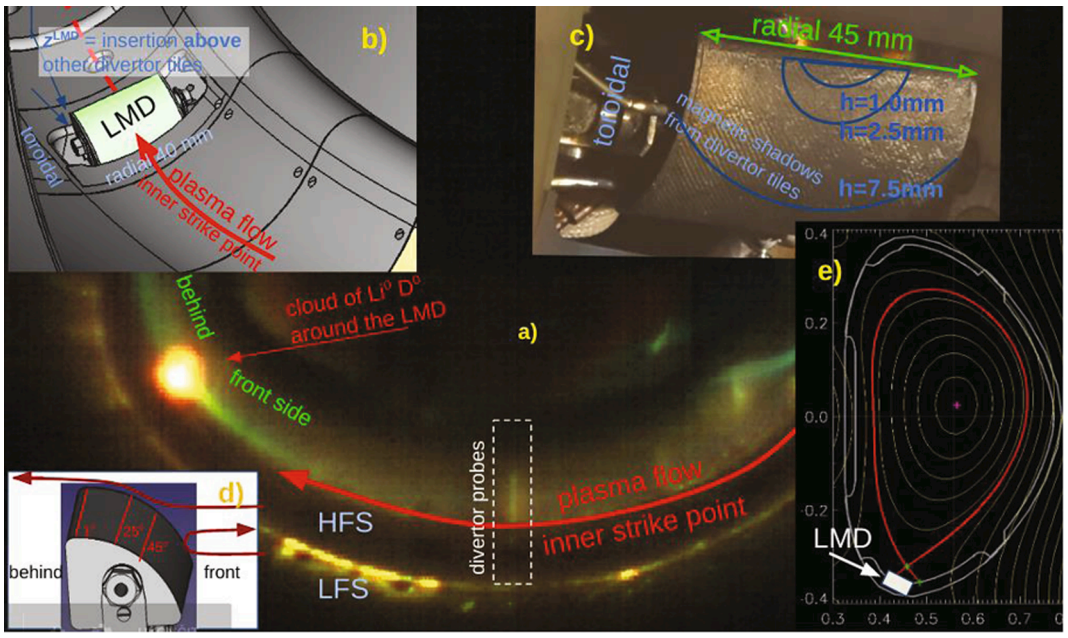

Fig. 1. a) Visible light camera view on the full graphite open divertor of COMPASS with the pure Li LMD target in #19781. b) schematic CAD drawing. c) Photograph of the LiSn target after 14 ELMy H-modes, showing no change from the photo before the campaign. The region of magnetic geometric shadow of the neighbor divertor tiles (3D-tracked by PFCFLUX) is marked by the blue circles for insertions (above the surrounding tiles) by $z^{LMD} = 1$, 2.5, and 7.5 mm. d) Heuristic scheme of why for deep insertion (i.e. high incident angle) and $p_{Li} > p_{e,deuterium}$ the Li flows to the front, against the plasma flow, whilst it is otherwise dragged by the plasma behind LMD. e) The poloidal cross-section showing the LMD position at the inner strike point. (For interpretation of the references to color in this figure legend, the reader is referred to the web version of this article.)

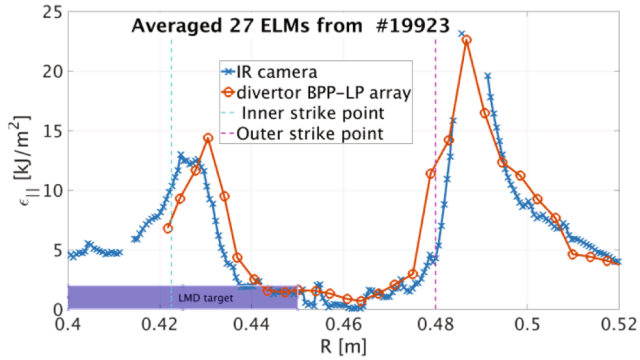

Fig. 2. Comparison of the divertor spatial profile of the parallel ELM-deposited energy fluence $= \int q_{dep} dt$ integrated over the ELM time ~0.2 ms. It is measured by IR camera or probes using $\gamma = 11$. Results from the outer target are consistent with what was found in [2,17].

1.41 eV to leave the surface. This cooling (and the vapor shielding cooling q_{vs}, see point **C**) is subtracted from the heating by the plasma as follows:

$$Q'_{dep} = q_{dep} - \Gamma^{Li}_{tot}(j_{sat}, T_e, T_{surface}) \cdot E_{vap} - q_{vs} \quad (1)$$

where q_{vs} is in (Eq.2). The lithium atom outflux from the target is estimated from $\Gamma^{Li}_{tot}(j_{sat}, T_e, T_{surface}) = (1 - R_{prompt}) \cdot ((Y_{preferential}(T_e) + Y_{thermal}(T_{surface})) \cdot j_{sat}/e + \Gamma_{vap}(T_{surface}))$, where

- **coefficient of prompt redeposition** $R_{prompt} = 0$ in COMPASS (see why in Section 4)
- **D plasma influx** $= j_{sat}/e$[ions/s/m^2], directly measured by the divertor probes at the same radial position (but far enough toroidally upstream to avoid mutual shadowing),
- **The preferential physical sputtering yield** $Y_{preferential}(T_e)$ (low but always present, independent on $T_{surface}$) is taken from [5],
- **The thermal physical sputtering yield** $Y_{thermal}(T_{surface})$ (dominates at intermediate $T_{surface}$) is taken from the adatom model [1]: $Y_{adatom}(T) = Y_{ad}/(1 + A \cdot exp(E_{eff}/k_B T_{surface}))$, where $Y_{ad} = 2.9$, $A = 9.6 \cdot 10^{-6}$, $E_{eff} = 0.7$ eV comes from the PISCES-B experiment [10],
- **The evaporation rate** (dominates at highest $T_{surface}$) is simply the *saturated vapor pressure* of either pure lithium $p_{v,Li}$[Pa] $= 10^{10.061 - 8023/T surface[K]}$ or tin $p_{v,Sn}$[Pa] $= 10^{10.268 - 15332/(T surface[K] + 80)}$ [4]. Note its extremely strong exponential dependence with $T_{surface}$ (increases by a factor of 10 each 70 K!). In order to be consistent with the more recent [29], we modified $T_{surface} \rightarrow T_{surface} + 80$ K. Recalculated by the Langmuir law to get the evaporation rate $\Gamma_{vap} = p_v(T_{surface}) \cdot (2\pi m_{Li} k_B T_{surface})^{-1/2}$ with vapor density $n_v = p_v/k_B T_{surface}$. For the LiSn alloy, Γ_{vap} writes approximately as $(\Gamma_{vap,Li} \cdot \Gamma_{vap,Sn})^{1/2}$ according to [29]. This evaporation rate is also consistent (except a shift by ~50 K) with [21]. If we used [21] instead, it would overall yield even lower Li evaporation rates $\Gamma_{vap}(T_{surface})$, thus lower cooling than shown in Fig. 4.

Surface temperature dependency of those three processes is shown in Fig.2.14 in [1].

It is worth mentioning that this cooling phenomena significantly reduces (>1 MW/m^2) q_{dep} only when $T_{surface}$ is higher than 900 °C for the LiSn alloy (which we marginally reached (Fig. 4c) thanks to the BNC used as a bulk material) or $T_{surface} > 600$ °C for the pure Li (which we did not reach due to high Molybdenum bulk heat conductivity and too short available discharge).

C. Vapor shielding [6] is the line-radiation of the excited lithium vapor cloud surrounding the target, which effectively cools down the incident plasma and forms a local lithium-induced detachment. Therefore, each released lithium atom cools down the plasma much more than by simply E_{vap}. Indeed, 7 eV $< \varepsilon_{cool}(\tau_{residence}, n_e, T_e) <$ 100 eV is the radiated energy according to Fig.3b in [13] taking into account all Li^0, Li^+, Li^{++} radiation losses. We thus calculate $\varepsilon_{cool}(time, space)$ from the

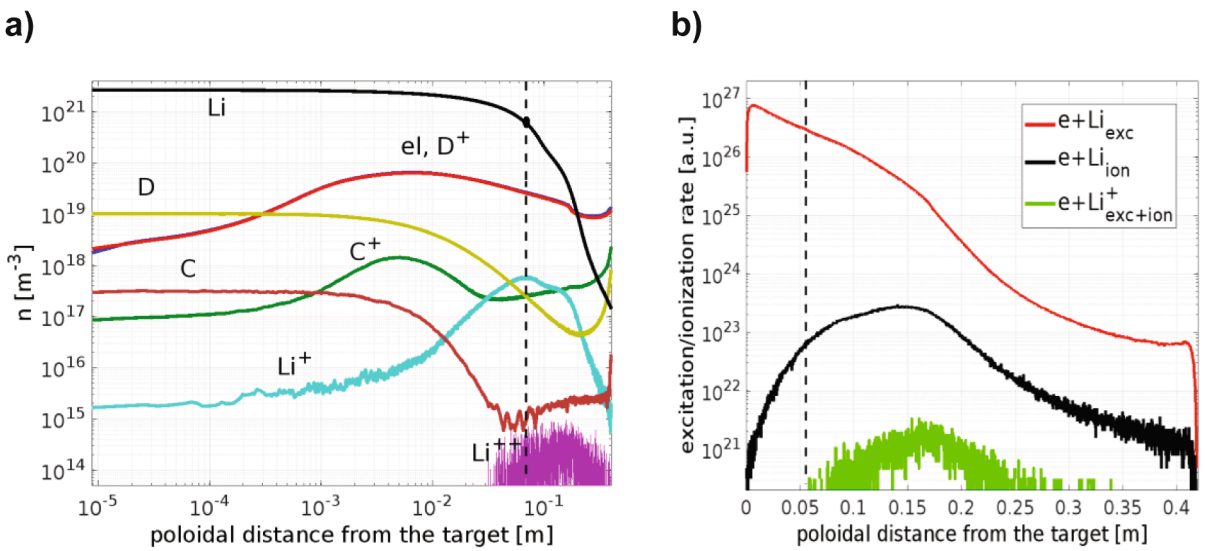

Fig. 3. Output from the PIC simulation of LMD evaporation + sputtering lithium. Consistently with what is found in Fig. 4d, $n_{Li} \sim 300 n_{e,deuterium}$ is also found here. a) Plasma density profiles, the dashed black line represents the position where Li density drops down to 1/e. b) Profiles of excitation (thus radiation) and ionization collision rate with e + Li corresponding to the red cloud and e + $Li^{+}_{exc+ion}$ to the green plume in Fig. 1a. (For interpretation of the references to color in this figure legend, the reader is referred to the web version of this article.)

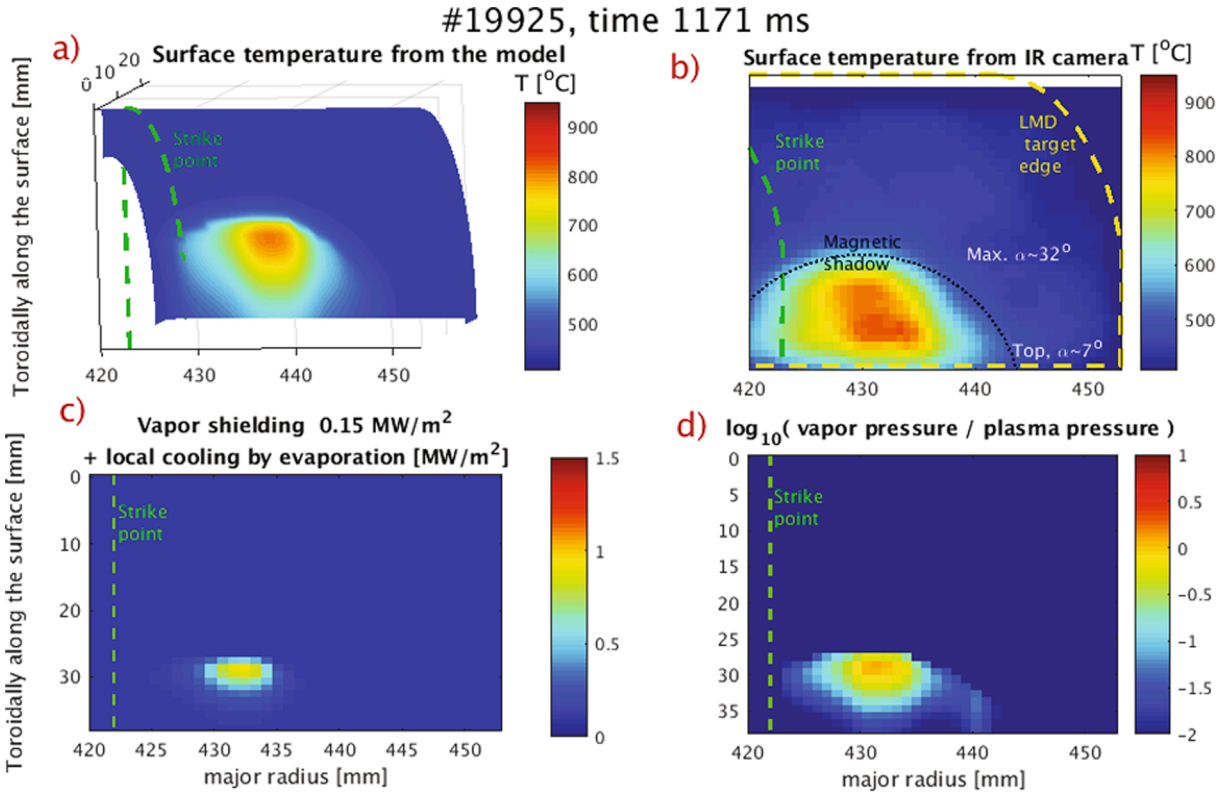

Fig. 4. Output of the simulation of the target. a) Time slice surface temperature from the heat conduction simulation (used to fill Table 2), b) surface temperature from IR camera with the magnetic shadow (black dashed line) estimated from PFCFLUX, c) total Li vapor cooling, d) normalized Li vapor to plasma pressures in logarithmic scale.

divertor probes. Since ε_{cool} also *weakly* depends on $\tau_{residence}$, we assumed the residence time to be $\tau_{residence} = L_{mfp}(2\pi m_{Li} k_B T_{surface})^{-1/2} \sim 10^{-4}$s, the typical time the lithium atom spends within the radiating cloud assuming no collisions. The simulation performed in Section 5.1 assuming so high and local vapor shielding would result in surface temperature rise similarly as in Fig. 5 only upto the moment when the plasma heat flux would balance with the (exponentially rising) radiating vapor cooling $\Gamma^{Li}_{tot} \cdot \varepsilon_{cool}$. This temperature limit would be 570 °C (assuming $R_{prompt} = 0$ according to the Section 4 simulation), 760 °C (assuming $R_{prompt} = 0.9$) or 820 °C (assuming $R_{prompt} = 0.99$). However, IR camera in Fig. 5 clearly observes continuous rise above 900 °C. This discrepancy is interpreted by the vapor cooling being non-local. Indeed, the *excitation/ionisation mean-free path* L_{mfp} is around 6 cm (see Section 4) which is much larger than the LMD vaporizing spot ($r_{vap.spot} \sim 4$ mm,

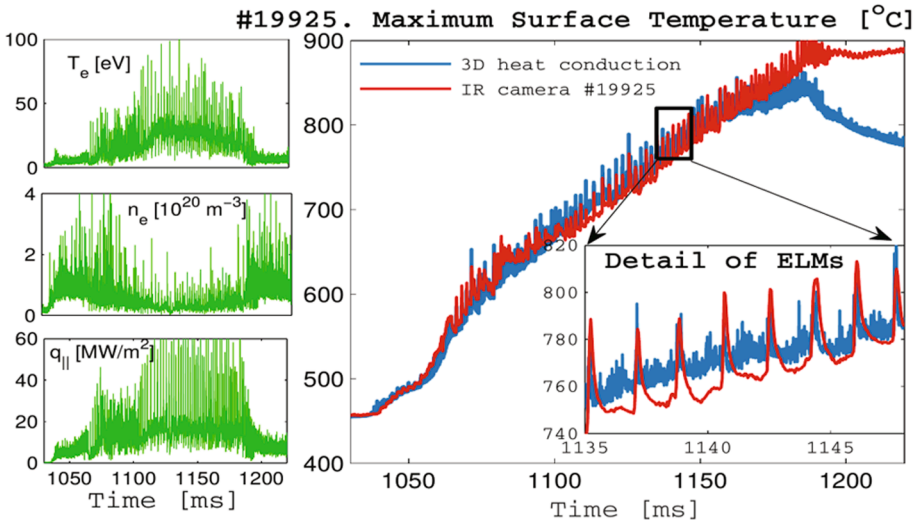

Fig. 5. Time evolution of the maximum LiSn LMD surface temperature (taken from Fig. 4a and b) directly measured by IR camera and from the heat conduction simulation in #19925 (deepest insertion) using $q_{||}$ from divertor probes (its signals at R = 430 mm are shown on left). Regular NBI-heated H-mode ELMs (expelling ~3% of stored plasma energy) deliver ~15 kJ/m^2, each heating the surface by ~40 °C.

see Fig. 4c). Note that approximately $4r_{vap.spot} = r_{hot\ spot} = \lambda_q^{divertor}$ due to the exponential dependence of p_{Li} on $T_{surface}$. This mechanism, therefore, cools down locally the incident plasma by only:

$$q_{vs}^{analytic} = \int_{LMD\ surface} \Gamma_{tot}^{Li} \varepsilon_{cool}\, dS / \pi L_{mfp}^2 \quad (2)$$

meaning that the lithium vapor shields a surrounding sphere which is $(r_{vap.spot}/L_{mfp})^2 \sim 100$ times larger than the vaporizing spot itself. At maximum, the model shows that the nonlocal vapor shielding reaches therefore only $q_{vs}^{analytic} = 0.15$ MW/m^2. This effectively yields the vapor cooling of the hot spot *weaker* than the latent heat of evaporation (mechanism **B**). However, for a hypothetical toroidally-continuous liquid metal divertor (the vapor box concept [13]), this vapor-cooled surface is not increased by $(r_{vap.spot}/L_{mfp})^2$ and therefore the vapor shielding should indeed become locally the dominant cooling mechanism.

4. BIT1 simulation of lithium prompt redeposition and the radiation cloud

In order to get more insight on the lithium evaporation, redeposition and transport in the vicinity of the target, a dedicated kinetic modeling via the Particle in Cell Monte Carlo code BIT1 [30] is further described. The simulation geometry corresponds to a 1D flux tube in the SOL adjacent to the separatrix and bounded by the inner and outer divertor plates. The model includes electrons, *D* and *C* atoms and D^+, C^+ impurities, plasma recycling and chemical sputtering of *C* with the sputtering coefficient taken as 0.01 (see [31] for more details). The main inputs of the simulation were the plasma density and the electron temperature at the outer mid-plane obtained from the Thomson scattering diagnostic: $n_e^{OMP} = 10^{19}$m^{-3}, $T_{e,OMP} = 60$ eV. The Li atoms are injected at the inner divertor with $\Gamma_{tot}^{Li} = 2.1{\times}10^{24}$ s^{-1}m^{-2} (corresponding e.g. to Fig. 4 at the end of the H-mode) and a temperature $T_{surface} = 0.09$ eV = 800 °C.

Obtained plasma and Li profiles, Li excitation and ionization collision profiles are plotted with respect to the poloidal distance from the target. First, Fig. 3 predicts that the radiating neutral lithium cloud has a radius of $L_{mfp} \sim 6$ cm (dashed black line). From the visible camera (see Fig. 1a), we indeed observe a (vapor shield) red cloud with comparable radius 2–5 cm (see also [8]). Results from Fig. 3a also indicate that the Li ionization front is located well above both the Li^+ gyro-radius (~30 μm) and the magnetic presheath (<1 mm), leading to negligibly small prompt Li re-deposition $R_{prompt} \sim 0$ at COMPASS (further assumed). It has to be noted that in the simulation we do not distinguish the prompt re-deposition from other re-deposition channels and $R_{total} < 10^{-3}$. This is in strong contrast to [27] where $R_{prompt} \simeq 0.99$ is used with the assumption that prompt redeposition is equal to total re-deposition. Second, assuming further that the radiation intensity is proportional to the number of inelastic (excitation and ionization) collisions, it can be concluded from Fig. 3b that e + Li excitation collisions represent the main radiation source. Note that plasma power loss in the vapor cloud evaluated from BIT1 simulation is 0.5 MW/m^2 for *#19925*. This is in rather good agreement with $q_{vs}^{analytic} = 0.2$ MW/m^2 obtained in the previous section.

5. Interpretation of experimental results

In this article, simulations of four representative discharges have been performed: three discharges with pure Li (2 with deepest insertion in L and H mode and 1 with target damaged) and one with LiSn (deepest insertion). The inputs and outputs of the simulations for these experiments are described in Table 2. In the next subsections, the simulation outputs are compared to the experimental observations made in these shots.

Here we shortly report on survival of the targets with respect to transient events such as ELMs and Vertical Displacement Events. For both targets, no droplet expulsed by those transients were observed. In fact, grounded current measurements show that ELMs yield a force of only 0.3 N/mm^2 and the downwards vertical displacement events yield force of only 0.4 N/mm^2 (because the plasma touches primarily the outer divertor target). Indeed, $j^{gnd}xB_t$ force dominates the droplet movement (see also [8]) and is two orders of magnitude lower than the capillary pressure [18]. In addition, during ELMs, a green plume is observed with visible cameras (see Fig. 6 left in [8]). It is a result of a sudden strong increase of evaporation rate (by a factor of 3 from the simulation), easily ionized by 5 times hotter ELM plasma ($T_{e,divertor,ELM} = 0.8T_{e,pedestal} \sim 200$ eV, see [3]).

Concerning the global plasma parameters, during both campaigns, we saw no consequences of the inserted LMD on plasma resistivity, line-average density nor the confined plasma temperature gradient (from Thomson scattering). In comparison to retracted target, insertion of the LMD resulted in no difference of the edge heat fluxes obtained by either midplane probes, divertor probes or divertor IR camera. Surprisingly, even the released droplets from the Li target (containing ~10^{19} atoms) caused no significant change on the divertor heat flux, even though it yielded huge radiation that locally saturated the visible camera. In the

Table 2
Principal inputs and outputs of the heat conduction model described in Section 3.

COMPASS LMD experiment	**#19781**	**#19803**	**#19805**	**#19925**
Diverted plasma mode	L	unstable H | L	similar to #19803	stable ELMy H (0.1 s)
liquid metal	lithium oxidized	lithium oxidized	lithium oxidized	LiSn
bulk material	Molybdenum	Molybdenum	Molybdenum	BNC ceramic
insertion z^{LMD}[mm]	7.5	4	5	2.5
max. sin(q) Fig. 2 in [8]	0.75	0.57	0.63	0.46
splashing droplets	no droplet	no droplet	many after 1250 ms	no droplet
q_{dep} [MW/m^2] peak | effective	18 | 17	18 | 12	similar to #19803	15 | 12
SIMULATION	⇑⇑ INPUTS ⇑⇑		⇓ ⇓ OUTPUTS ⇓⇓	
max. $T_{surface}$ [°C]	IR saturated 650 simulation	IR saturated 520 simulation	~2600 from visible camera	900 IR-camera 850 simulation
max. Li local vapor cooling [MW/m^2]	~0.3 by thermal sputtering	~0.3 by thermal sputtering	no data	1.0 by evaporation
max. Li nonlocal vapor shielding q_{vs} [MW/m^2]	0.5 dominated by thermal sputtering	0.1 dominated by thermal sputtering	no data	0.15 analytic dominated by evaporation BIT1 yields 0.5
total vaporized lithium 10^{19} atoms	0.1	0.01	no disruption but the CPS mesh **melted** (**damaged**) likely due to the solid *LiO* layer	0.4 in H-mode 1.5 (total)
max. n_{Li}/n_e	~200	30		300-1000
***max.* p_{Li}/p_e**	~1 after 1.18s	0.1		3

Li-campaign, only about 0.5 g of Li locally splashed. In the entire LiSn-campaign it evaporated only 1 mg in total according to the model in Section 3. According to [7], for a visible effect on the global plasma parameters we estimate around 1 g of Li homogeneous coating of the vacuum vessel would be required.

5.1. LiSn alloy wetted on thermally-insulating LMD

The main output of the heat conduction simulations presented in Section 3 is the time evolution of the whole target surface temperature, calculated from heat fluxes measured by divertor probes (1 MHz). Comparing the target hot spot simulated in Fig. 4a at the end of the stable ELMy H-mode of #19925 and the one measured by IR camera in Fig. 4b, one can notice qualitative agreement (maximum temperature value) but a minor mismatch at the LMD target top location, where the plasma heat flows parallel to the surface ($\sin(\alpha) \sim 0$). There, our model naturally expects zero temperature rise, whilst IR camera observes strong heating. This mismatch observed for all shots is possibly due to the ion Larmor smoothing around the target magnetic shadow.

In Fig. 5, the evolution of the simulated maximum target temperature is compared to the one measured by the IR camera. It is clearly seen that the model surface temperature rise is consistent with the measurements. It shows the simulation parameters (c_v and $\boldsymbol{\kappa}$) in Table 1 are correct. The simulation also matches the ELM temperature $\Delta T^{\mathrm{ELM}}_{\mathrm{surface}}$ rise only thanks to using finite heat transmission coefficient [35] set to 1 MW/m^2/K which characterises the LiSn poorly-conductive layer (much thinner than the 1 mm-thin CPS). The simulation ran without assuming such a layer yields $\Delta T^{\mathrm{ELM}}_{\mathrm{surface}}$ of few Kelvins only. In the simulation, there is, however, one unresolved observation: After back transition to L-mode (after 1180 ms), the strike point moves by 15 mm (approximately one divertor heat flux decay length), yielding to a temperature drop according to the simulation, whilst according to the IR camera, the temperature keeps slowly rising.

Last, the simulated Li pressure exceeded the deuterium one by a factor $10^{0.5} = 3$ (Table 2), as seen in Fig. 4d, leading to a total cooling around 1.15 MW/m^2 (Fig. 4c) with 1 MW/m^2 from the mechanism **B** and 0.15 MW/m^2 from the mechanism **C**. Since this cooling is much lower than the plasma heat flux, the equilibrium was evidently not reached in this experiment.

5.2. Lithium wetted Molybdenum LMD

In the #19781 L-mode, the Li target was inserted up to 7.5 mm with effectively $q^{\mathrm{probes}}_{\mathrm{dep}} = \frac{3}{4} q_{||} = 17$ MW/m^2 during the longest-possible 0.2 s flattop period with stable strike point, reaching thus 600 °C on the surface (according to the simulation since the IR camera was saturated at 400 °C). Just above the surface, the simulated neutral lithium density rose to approximately $n^{\mathrm{Lmode}}_{\mathrm{Li}}/n_{\mathrm{e}} \sim 200$ times the plasma density and p_{Li}

$\sim p_e$ is found for t > 1.18 s. As indirect proof of such high pressure, we indeed observed a green plume of Li^+ start to appear for t > 1.18 s *in front* of the target, whilst otherwise it is always observed *behind* the target (see the green plume in Fig. 1a). As sketched in Fig. 1d, such phenomena could be explained by the lithium pressure overcoming the plasma pressure, so that ionized lithium atoms could diffuse against the plasma flow. The authors believe that, when the target is deeply inserted, the pressurized Li gas can diffuse only against the flow (since the flow is blocked by the target itself), explaining the front green plume in #19781 ($z^{LMD} = 7.5$ mm), whilst at the top location the plasma flow may dragg the Li atoms behind the target, explaining why no front green plume was observed in #19925 ($z^{LMD} = 2.5$ mm), even though $p_{Li} \sim 3p_e$.

In the #19803 H-mode, even though it also reached up to 18 MW/m^2 for several 5–10 ms periods, the target was effectively only exposed to 12 MW/m^2 during 0.2 s due to strike point movement. In addition, due to the high conductivity of the Molybdenum bulk, the simulation shows that the surface reached only 520 °C in the most exposed ELMy H-mode and that the surface released only 10^{17} lithium atoms (mostly from thermal sputtering, mechanism **B**) from the hot spot of 20x7 mm^2 size. The lithium cloud density was therefore smaller than in L-mode: $n_{Li}^{Hmode}/n_e^{Lmode} \sim 30$.

In #19805 at 5 mm insertion, the target unexpectedly lost the lithium protective layer and the *Mo* mesh catastrophically melted. Its negligible heat capacity (0.1 mm thin wires with negligible heat contact to the bulk) theoretically melts [23] within 50 ms. We indeed observed by the color visible camera a visibly glowing hot surface after plasma termination. From the ratio of camera color pixels (red/green/blue, assuming black-body radiation and color-independent emissivity), $T_{surface}$ was around the Molybdenum melting point after the plasma discharge ended. In several subsequent discharges we observed strong Li splashing from this damaged region (even explosive droplet ejection by boiling *Li*) and the Li *did not refill* the dried out surface (perhaps due to boiling Li and mesh thermal expansion by $\Delta T \sim 2500$ K). We verified the following possible reasons for its damage:

- Lack of lithium liquid was not observed because still there was 3 cm^3 left in the reservoir after the campaign.
- Bending of the *Mo* mesh (which could prevent downwards thermal contact) was not observed because the thermal expansion of the previous shot *#19803* was only 350 K·6·10^{-6}/K·$r_{hot\ spot}$ = 0.05 mm which is less than the *Mo* wire thickness. Thus the stress could be easily absorbed by lateral mesh expansion.
- The presence of the oxidized solid layer may be the reason because we observed (by its much lower emissivity) progressive sputtering of the oxidized solid layer at some regions during 20 previous discharges and it may have been oxidized deeply inside the CPS mesh which prevented the liquid Li to wet the surface.

6. Summary

Two small liquid metal targets based on the capillary porous structure and filled by pure lithium and a lithium-tin alloy were exposed to the divertor plasma of the tokamak COMPASS in two separate experiments. We observed no influence of both experiments on the Deuterium plasma, except very intensive Li radiation from droplets from the Li target edge only (expelled likely due to Li-oxidized layer). The LiSn target was exposed to surface-perpendicular plasma heat flux up to 12 MW/m^2 for 0.2 s, reaching 900 °C after 0.1 s of H-mode with Type-I ELMs, yielding no liquid splashing even though each ELM raised the surface temperature by ~40 K and delivered Lorentz pressure $j_{ground} x B_{toroidal} \sim 300$ kPa. We observed a lot of evaporated Lithium but no Tin. We developed a dedicated model of 3D heat conduction (with heat and particle flux input either from divertor probes or IR camera) in the solid body, determining the surface temperature and thus the Li sputtering and vapor shielding for both experiments. This model suggests that in the LiSn target case the lithium vapor density exceeded locally the plasma density by factor of 1000 (and the pressure by factor of 3). For the pure Li target at deep insertion we saw indication of lithium diffusing also against the plasma flow just when $p_{Li}/p_{Deuterium} > 1$. Our PIC simulation calculates the ionization mean-free 6 cm, implying zero lithium prompt redeposition. The latent heat of Li vapor cools down by <1 MW/m^2. The evaporated + sputtered lithium shields the incident Deuterium plasma heat flux within a sphere (of radius ~6 cm indeed observed by the visible camera) around the vaporizing hot spot (~4 mm size), therefore cooling large surrounding areas, not only the hot spot. Effectively, the Li vapor shielding thus stays below 0.2 MW/m^2. Therefore the LMD target temperature *did not* (due to 0.1 s short discharge) reach equilibrium in which plasma heating and cooling by the vaporized lithium would be in balance.

Declaration of Competing Interest

The authors declare that they have no known competing financial interests or personal relationships that could have appeared to influence the work reported in this paper.

Acknowledgments

We appreciate suggestions from T.W. Morgan, M. Jaworski, F. Tabares and technical help from V. Veselovsky, Mathis Feuvrie and Adrien Abrassart from ENSAM (internship). Oost acknowledges for the partial financial support from MEPhI and NRU MPEI in the framework of the Russian Academic Excellence Project. Participation of A. Prishvitcyn, Y. Gasparyan and Y. Vasina was partly supported by the Russian Foundation for Basic Research (grant 18-32-20114\18). This work has been carried out within the framework of the projects COMPASS-U: Tokamak for cutting-edge fusion research (No. CZ.02.1.01/0.0/0.0/16_019/0000768) and co-funded from European structural and investment funds. This work has also been carried out within the framework of the EUROfusion Consortium and has received funding from the Euratom research and training programme 2014–2018 and 2019-2020 under grant agreement No 633053. The views and opinions expressed herein do not necessarily reflect those of the European Commission. This work was co-funded by the MEYS projects 8D15001 and LM2018117 and part of the Czech Science Foundation project GA20-28161S.

References

[1] ABRAMS, T.W. Ph.D. thesis, Princeton University, 2015.
[2] J. Adamek, et al., Nucl. Fusion 57 (2017), 116017, https://doi.org/10.1088/1741-4326/aa7e09.
[3] J. Adamek, et al., Nucl Fusion 60 (2020), 096014, https://doi.org/10.1088/1741-4326/ab9e14.
[4] C.B. Alcock, et al., Canadian Metall. Q. 23 (1984) 309.
[5] R. Behrisch, W. Eckstein, Topics in applied physics 110, Springer Verlag, Berlin, 2007.
[6] J. Cecrdle, Bachelor thesis, Czech Technical University (2019).
[7] Y. Chen, et al., Plasma Phys. Control. Fusion 57 (2015) 025012, https://doi.org/10.1088/0741-3335/57/2/025012.
[8] R. Dejarnac, et al., Nuclear Materials and Energy 25 (2020) 100801, https://doi.org/10.1016/j.nme.2020.100801.
[9] P.D. Desai, J. Phys. Chem. Ref. Data 16 (1987) 91, https://doi.org/10.1063/1.555794.
[10] R.P. Doerner, et al., J. Nucl. Mater. 166 (2001).
[11] T.B. Douglas, et al., J. Am. Chem. Soc. 77 (8) (1955) 2144–2150.
[12] T. Eich, et al., Nucl. Fusion 53 (2013), 093031, https://doi.org/10.1088/0029-5515/53/9/093031.
[13] R.J. Goldston, Nucl. Mater. Energy 12 (2017) 1118, https://doi.org/10.1016/j.nme.2017.03.020.
[14] A. Herrmann, et al., Plasma Phys. Control. Fusion 37 (1995) 17.
[15] J. Horacek, et al., Fusion Engineering and Design 123 (2017) 646–649, https://doi.org/10.1016/j.fusengdes.2017.01.027.
[16] J. Horacek, et al., Plasma Physics Reports 44 (7) (2018) 652–656, https://doi.org/10.1134/S1063780X18070024.
[17] J. Horacek, et al., Nucl. Fusion 60 (2020), 066016, https://doi.org/10.1088/1741-4326/ab7e47.
[18] M.A. Jaworski, et al., Nucl. Fusion 53 (2013), 083032, https://doi.org/10.1088/0029-5515/53/8/083032.

[19] M. Komm, et al., Nucl. Fusion 59 (2019), 106035, https://doi.org/10.1088/1741-4326/ab34d2.
[20] M. Komm et al., submitted to Nuclear Fusion.
[21] M. Kondo, Y. Nakajima, Fusion Eng. Design 88 (2013) 2556–2559. https://linkinghub.elsevier.com/retrieve/pii/S0920379613004894.
[22] V.P. Krasin, S.I. Soyustova, High Temp. 57 (2) (2019) 190–197. https://10.1134%2FS0018151X1902010X.
[23] S. Lukes, Bachelor thesis, Czech Technical University (2020).
[24] T.W. Morgan, et al., Plasma Phys. Control. Fusion 60 (2018), 014025, https://doi.org/10.1088/1361-6587/aa86cd.
[25] R.A. Pitts, et al., Nuclear Materials and Energy 20 (2019), 100696, https://doi.org/10.1016/j.nme.2019.100696.
[26] Plansee material properties. https://www.plansee.com/en/materials/molybdenum.html.
[27] P. Rindt, et al., Nucl. Fusion 58 (2018), 104002, https://doi.org/10.1088/1741-4326/aad290.
[28] S. Sharafat, N. Ghoniem. APEX Study University of California Los Angeles, 2000.
[29] F.L. Tabarés, et al., Nucl. Fusion 57 (2017), 016029, https://doi.org/10.1088/0029-5515/57/1/016029.
[30] D. Tskhakaya, Plasma Phys. Control. Fusion 59 (2017), 114001.
[31] D. Tskhakaya, et al. this conference.
[32] P. Veis et al. this conference.
[34] A. Vertkov, et al., Plasma Physics Reports 44 (7) (2018) 664, https://doi.org/10.1134/S1063780X18070073.
[35] P. Vondracek, et al., Fusion Engineering and Design 146A (2019) 1003–1006, https://doi.org/10.1016/j.fusengdes.2019.01.142.
[36] R. Wenninger, et al., Nucl. Fusion 55 (2015), 063003, https://doi.org/10.1088/0029-5515/55/6/063003.
[37] R. Wenninger, et al., Nucl. Fusion 57 (2017), 046002, https://doi.org/10.1088/1741-4326/aa4fb4.
[38] J. Wesson Tokamaks, et al., Book, 3rd edition, Oxford University Press, 2004.
[39] Mazzitelli, et al., Journal of Nuclear Materials (2015) 1152, https://doi.org/10.1016/j.jnucmat.2014.12.050.
[40] Eich, Nuclear Materials and Energy 12 (2017) 84, https://doi.org/10.1016/j.nme.2017.04.014.
[41] R Pitts A, Nuclear Materials and Energy 12 (2017) 60, https://doi.org/10.1016/j.nme.2017.03.005.